Journal of
Materials Chemistry B

Materials for biology and medicine

Accepted Manuscript

This article can be cited before page numbers have been issued, to do this please use: N. Rossberg, S. R. Corrie, L. Grøndahl and I. Jayawardena, *J. Mater. Chem. B*, 2025, DOI: 10.1039/D5TB00848D.

ROYAL SOCIETY OF CHEMISTRY

rsc.li/materials-b

View Article Online
DOI: 10.1039/D5TB00848D

Automated Analysis of Pore Structures in Biomaterials

Nicola Rossberg[1], Simon Corrie[2], Lisbeth Grøndahl[3] and Imanda Jayawardena[4]*

1. Taighde Éireann - Research Ireland Center for Research Training in Artificial Intelligence, School of Computer Science & Information Technology, University College Cork, Co. Cork T12 K8AF, Ireland.
2. Chemical and Biological Engineering Department, ARC Centre of Excellence in Carbon Science and Innovation, Monash University, Clayton, VIC 3800, Australia.
3. School of Chemistry and Molecular Biosciences, University of Queensland, Brisbane, QLD 4072, Australia.
4. Tyndall National Institute, Lee Maltings Complex, Dyke Parade, Cork, Co. Cork T12R5CP, Ireland.

Abstract

Quantitative assessment of pore size and morphology is crucial in biomaterials design and evaluation, particularly hydrogels and scaffolds used in tissue engineering and drug delivery. In recent years, a growing number of studies have proposed or adopted automated image analysis tools to evaluate pore characteristics; however, the absence of standardised protocols, validation criteria, and consistent reporting practices has limited reproducibility and cross-study comparability. This perspective, for the first time, examines recent trends in automated pore size analysis in biomaterials research, highlighting commonly used algorithms, their implementation in image-based workflows, and their ability to resolve pore geometries in disordered materials. We discuss the influence of imaging dimension, resolution, algorithm assumptions, and image pre-processing on outcomes and highlight common challenges such as over-segmentation, user bias, and the misidentification of irregularly shaped pores. By drawing on selected examples from the literature, we illustrate both the strengths and limitations of current approaches and emphasise the need for transparent, standardised methodologies in the field.

Keywords: Biomaterials, pore size, mesh size, imaging, automated methods, machine learning, artificial intelligence

1. Introduction

Porous materials, particularly hydrogels and scaffolds, have widespread uses in biomedical applications where the pore structure is a key determinant of functionality. The porosity, pore size distribution, and pore interconnectivity of these materials influence critical properties such as mechanical strength, degradation rate, fluid transport, and biological interactions[1–5]. Accurate pore characterisation is essential for optimising biomaterials for applications such as tissue engineering (affecting cellular adhesion, proliferation, and differentiation[6,5,7,8]), drug delivery (affecting release kinetics[9,10]), and biosensing (affecting molecular diffusion and sensor performance[11]).

View Article Online
DOI: 10.1039/D5TB00848D

In hydrogel-based materials, mesh size (the space between crosslinking sites in polymer chains) and mesh radius (size of largest spherical solute that could move through a mesh portal) governs mechanical properties and permeability of the material, whereas pore size (the voids within e.g. hydrogel network or scaffold) plays a crucial role in cellular infiltration, nutrient diffusion, and tissue regeneration[1,5,7,12–17]. Hydrogels with small mesh sizes provide higher mechanical stability but may restrict cellular infiltration, whereas larger pores enhance cell migration and diffusion but can compromise mechanical integrity[1,7,18]. Similarly, scaffold-based biomaterials rely on optimised pore architectures to balance mechanical support with biological functionality[1,5,8,19].

Traditional methods for characterising pore structures, such as manual analysis from images are time-intensive, and are prone to over or under estimation of parameters, subjectivity and bias[1,3,5,20,16]. These methods often fail to provide comprehensive characterisation, particularly for hydrogels, which have hydrated and dynamic porous networks. While semi-automated approaches have been developed, limitations such as bias during user input, low sample sizes during verification steps and lack of accessibility to both software and sample measurement techniques has necessitated automation[3,5,20,21]. As a result, there has been an increase in adopting automated pore analysis techniques that utilise advanced image processing and artificial intelligence (AI) algorithms[1,10,20,22–24]. Automated segmentation and feature extraction enable high-throughput, reproducible, and quantitative analysis of pore architectures across various length scales[25]. Furthermore, automated models can enhance image contrast, remove noise, and classify pore structures with minimal human intervention[7].

Numerous studies in the literature develop and/or use automated methods for pore size analysis. However, in the absence of standardised methodologies, reporting guidelines, or benchmarking criteria, comparison across different materials becomes challenging. It is therefore important to evaluate studies from the current literature to illustrate such limitations and strengths. This perspective is, to our knowledge, the first to provide a focused and critical evaluation of automated pore size analysis methods as applied to biomaterials such as hydrogels and porous scaffolds. We explore various automated approaches used to quantify pore characteristics from images recorded using direct two- dimensional (2D) and three-dimensional (3D) imaging methods, discuss the challenges associated with analysing disordered porous materials, and provide recommendations for future developments in automated pore analysis.

2. Background to Porous Materials

2.1 Defining Pores in Literature

The term "pore" is widely used across materials science but lacks a universal definition due to variations in material structures and measurement techniques. In biomaterials, a pore is generally defined as a void or cavity within a solid or gel matrix that facilitates fluid transport, gas diffusion, or cellular infiltration[2,26]. Pores can exist at multiple length scales, ranging from macropores (>50 nm), which promote cell migration and vascularisation, to mesopores (2-50 nm), which control molecular diffusion in drug delivery systems[27].

In polymeric biomaterials, such as hydrogels, mesh size refers to the distance between crosslinking sites in polymer chains, mesh radius[28] describes the voids within a polymeric network, while pore size[2] is the area of void space within solid material where the structures

View Article Online
DOI: 10.1039/D5TB00848D

separating the void spaces (e.g. pore walls) consists of polymer bundles. The latter is the pores that can be visualised using images captured using various techniques.

2.2 Classification of Materials Based on Pore Structure

Biomaterials exhibit a wide range of pore architectures ranging from cubic to irregular shaped as illustrated in Figure 1. They may present almost entirely of one type of pore architecture arranged in an ordered pattern and hence be categorised as ordered structures. Examples of this include silicas, metal–organic frameworks (MOF)s, Zeolites, and crystalline porous materials, and directly relevant to this perspective, ordered scaffolds[29–34]. These materials possess highly uniform and regularly spaced pores, making them ideal candidates for automated image analysis using segmentation, machine learning-based pattern recognition, and feature extraction[35,36].

Alternatively, biomaterials may have a mixture of different pore architecture and/or irregular arrangement of pores and as such can be categorised as a disordered structure. It should be noted that not only the pore structure but also the pore walls may be variable across a disordered structure. Disordered structures such as disordered scaffolds[8,16,18,19,37], hydrogels[2,7,13,38–40] and fibrous networks[8,17,24,25,39,41–44] are examples of this and they are comprised of inherently irregular and porous architecture, making automated characterisation challenging. Automated methods, such as micro-computed tomography (micro-CT), 3D image reconstruction and AI-based segmentation models, have been used to analyse these architectures[10,26].

Figure 1: 2D and 3D pore architectures in biomaterials.
All images have been reproduced with permission.
A: Left: How a pore is defined in a 2D image[2]. Right: Graphical representation of pore size calculation and slices used in a 3D reconstruction[45].
B: Left: 3D visualisation of pores detected as spherical bubbles: Orange depicts segmented collagen fibers and blue represents pores. Right: 2D visualisation (circles) of detected 3D bubbles in the left image, in an exemplary 2D image slice. Black depicts segmented collagen fibers, blue represents determined pores of a single analysis process, orange represents detected pores of a second residual analysis[16].
C: Top left corner and centre: Scanning electron microscopy (SEM) images of salt leached and gas foamed scaffolds[3]. Top right centre: Scanning electron micrograph of the microfluidic foaming poly(vinyl alcohol) (PVA) scaffold[45]. Top right corner: FESEM images of electrospun poly(l-lactic acid)-co-poly(ε-caprolactone)-Gelatin (PLACL/Gel) nanofibers[37]. Bottom left corner: SEM micrographs of a PCL scaffolds produced by bioextrusion[15]. Bottom left centre: Micro-CT 2D section of a collagen-based composite scaffold[46]. Bottom right centre: Confocal fluorescence microscopy image of a collagen network[47]. Bottom right corner: SEM image of an agarose hydrogel[2].
D: 3D bubble method applied to an in silico fibrin gel. Left: Red spheres represent the largest 3D bubbles that can be optimally fit in the pore zones of the gel and produce their maximum filling. Right: Zoom of a single sphere touching four different fibers[17].
E: Left: Synchroton micro-CT image of a bioactive glass scaffold. Right: Pores within the scaffold identified by image analysis algorithms[48].

This perspective primarily focuses on disordered porous materials, such as hydrogels and scaffolds, where variability in pore shape, size, and connectivity complicates standard pore characterisation techniques[38]. However, understanding how automated methods have been

View Article Online
DOI: 10.1039/D5TB00848D

applied to ordered porous structures, such as mesoporous silica and MOFs, whether successfully or with limitations, facilitates their adaptation for more complex materials[1,16,29,35].

3. Automated Image Processing Techniques for Pore Analysis

3.1 2D and 3D Imaging Methods

A key distinction in pore analysis is between 2D and 3D imaging techniques, as each approach presents unique challenges and limitations (Figure 1C). Traditionally, pore size analysis relies on 2D imaging (Figure 1C), where threshold functions enhance pore or fiber structures, improving visibility and signal-to-noise ratio[12,13,49]. However, this method remains subjective due to a lack of benchmarking, reliance on user input, and qualitative assessment[5,16]. Additionally, factors such as resolution, background noise, and focus variations across imaging modalities can further impact accuracy[5,16]. These limitations have driven the development of more advanced, automated approaches.

A fundamental challenge of 2D pore analysis is its inability to capture the true three-dimensional pore architecture. For instance, scanning electron microscopy (SEM) images (literature examples provided in Figure 1C, 2F, 3C) captured using a high resolution technique have inherent limitations; including restricted planes of view due to fractured surfaces examined by SEM, minor pores being unclear or easily overlooked, challenges when imaging multilayered biomaterials, and lack of standardised protocols for improved robustness and limiting user-bias during pore quantification[19,43,46,47]. Circular or elliptical pore cross-sections in 2D may misrepresent actual 3D pore connectivity, requiring stereological or computational corrections[17,19,20,50]. Moreover, orientation dependence and sampling bias introduce further inaccuracies, particularly in fibrous or interconnected scaffold structures[17,46]. Pore shape is crucial, because unless specifically engineered to achieve a highly ordered shape, pores are irregularly shaped (Figure 1), thus physical or virtual sectioning anywhere other than where the pore diameter is maximum (Figure 1A) leads to an underestimation of pore size[2,28,46]. This is also influenced by the threshold chosen for the sample and imaging artefacts/tilts/curvatures, requiring filtering and segmentation to improve the accuracy of pore boundary determination[50]. While statistical sampling methods, such as unbiased stereology are used to approximate 3D characteristics, they may not be suitable for highly interconnected porous networks[17].

3D imaging techniques, such as micro-CT, confocal laser scanning microscopy (CLSM), transmission electron microscopy (TEM) tomography reconstruction and focused ion beam SEM (FIB-SEM), have been used for obtaining non-destructive, high-resolution information regarding pore morphology[28,43,47] (Figure 1B, D, E, 2A, B, D, 3A, B). The convoluted data and naturally complex biological networks make manual data extraction from confocal images challenging, driving automation[17]. Furthermore, a resolution and volume interdependence for TEM tomography and FIB-SEM have been reported[51]. Micro-CT (Figure 1E, 2B, 3A), in particular, enables quantitative assessment of porosity and connectivity, linking these parameters to material function[20,47]. Further, the technique allows virtual sectioning, visualisation in different planes and colour coded visualisation for improved comprehension[46]. However, the accuracy of 3D segmentation relies on grayscale differentiation and thresholding, which are often subjective and affected by environmental

View Article Online
DOI: 10.1039/D5TB00848D

factors such as lighting and computer monitor resolution and personal factors such as fatigue[20,27]. 3D methods often acquire repeated 'slices' of a 3D material, process them in a 2D format and aggregate to reconstruct the 3D image. Furthermore, the high cost and low accessibility of micro-CT, especially for nanometre level visualisation, computational intensity and data scarcity for machine learning-based 3D segmentation further complicate widespread adoption[17,20,38,43,52]. As noted by Mickel et al. ‘a generic definition (for pore size) and a robust method to extract pore sizes from experimental three-dimensional microscopy data sets have been lacking’[53].

Regardless of imaging method, 2D or 3D, quality of the source image is a key determinant of the resultant pore size metrics, and in manual image analysis methods in particular, there is a trade-off between accuracy and time and effort[47,52]. Studies directly comparing 2D vs. 3D pore analysis have shown systematic discrepancies (% discrepancy) in extracted values, with 2D methods often underestimating porosity and connectivity[38,54]. Given these challenges, hybrid approaches, combining stereological corrections with machine learning-assisted 3D reconstruction, are emerging as promising solutions[52].

As we focus on direct 2D and 3D imaging techniques, the accuracy of pore quantification relies on automated image processing techniques that extract meaningful information from images. This section discusses the segmentation process (to isolate pores from the surrounding material) in Table 1, Box 1 and Table 2, and pore analysis techniques (to quantify pore characteristics) in Box 2 and Table 3. Given the complexity of porous materials, different approaches, ranging from thresholding-based methods to machine learning-driven segmentation[10], have been developed to improve accuracy and reproducibility in pore characterisation[1]. It is important to note that the suitability of the algorithms will vary as a function of the considered biomaterial and imaging modality. Depending on the available equipment, the signal-to-noise ratio and contrast, separation of background and specimen and image resolution will vary, changing the task difficulty, accuracy and consequentially the choice of segmentation and analysis approach[47,54,55].

3.2 Segmentation: Extracting Pores from Images

Segmentation is the first step in automated pore analysis, where the material and pores are distinguished as separate entities. Examples of segmentation methods used in the literature are given in Figure 2. The choice of segmentation technique directly impacts the quality of extracted pore features and should be as close to ‘ground-truth’ as possible. Due to the range of imaging modalities and factors such as background lighting and noise, the choice of segmentation technique is imperative to effectively visualise pores. To evaluate segmentation success, an objective ‘ground-truth’ comparator is required. However, at the moment, ‘ground-truth’ is frequently established through manual measurement and inter-rater reliability which introduces bias and is subject to fatigue effects for large sample sizes[45,56]. Due to the associated effort, reliance on automated segmentation and analysis approaches without ‘ground-truth’ validation is increasing[46]. Automated methods, including methods discussed below in Box 1, offer standardised, reproducible segmentation but may still misclassify features, over-segment noise or under-segment adjacent pores (Figure 2). While these methods are thus more time effective and objective than manual approaches, their lack of validation presents a new risk of bias[27]. Hybrid approaches, combining automated segmentation with manual refinement, could be a balanced approach, however, would require pre-processing steps such as contrast enhancement and noise reduction (as outlined in Table

View Article Online
DOI: 10.1039/D5TB00848D

1) to improve the accuracy of pore boundary detection. Table 1 details several preprocessing steps to improve the efficacy of image-based segmentation and analysis.

Table 1. Examples of preprocessing steps in segmentation

Pre-processing Modality	**Purpose**	**Software for Implementation**
Edge Detection	Allows the separation of touching objects without specifying a subjective threshold[52].	ImageJ / MatLab / OpenCV
Contrast Maximisation	Maximises the contrast between pores and walls or pores and the background to ease segmentation and analysis[21].	ImageJ / MatLab / OpenCV
Despeckling	Despeckling sweep removes all but the largest objects in a space. Despeckling sieve removes objects below a certain area or volume. Adaptable for 2D or 3D space[57].	ImageJ
Morphological Operations	Operations that can analyse and modify image shapes and structures. Can also be implemented for noise removal and feature extraction[18,19,21,24,45,52,54].	Image J / MatLab / Quanfima python package[24]
Gaussian Blur	A technique to smooth an image by averaging pixel values within a Gaussian window, effectively reducing noise[58,59].	ImageJ / MatLab / OpenCV / Scikit – image package for python
Anisotropic Diffusion Filtering	Reduces noise while preserving edges by allowing diffusion to occur primarily in homogenous regions[60].	ImageJ / MatLab / MedPy Python Package
Mean / Median Filtering	Reduces noise by replacing each pixel's value with the mean or median value of the surrounding pixels[12,19,25].	ImageJ / MatLab / SciPy Python Package / OpenCV

In Box 1, we outline a range of (semi-)automated segmentation approaches. Thresholding is the simplest and most widely used segmentation technique, where pixels are classified as either pore or material, based on intensity values (Figure 2). Thresholding-based segmentation is computationally efficient but may struggle with detecting intricate pore networks, particularly in fibrous or highly porous materials[43]. Additionally, it may yield variable results due to user-defined parameters and a lack of benchmarking[20,27]. Machine learning (ML) techniques, both shallow learning (e.g., support vector machines, decision trees) and deep learning (e.g., convolutional neural networks (CNN), U-Net models), can be used for pixel-wise classification in pore segmentation[5,20,61–63,39]. However, machine learning is data-hungry, thus requiring larger sample sizes and manual 'ground-truth' labelling which is labour intensive and may introduce user-bias into the segmentation process.

Box 1: Segmentation Approaches

📌 Thresholding-Based Approaches

- **Global Thresholding**: A single threshold is applied across the entire image, making it suitable for materials with uniform contrast but less effective for heterogeneous structures[3,47,64–66,56,21,1,38,8,67,43,52]. These techniques are also more sensitive to noise[68]. Some examples of global thresholding methods are given

View Article Online
DOI: 10.1039/D5TB00848D

below, more methods and an in-depth discussion on thresholding could be found through Rajagopalan et al.[27]

- **Otsu's Global Thresholding:** Selects an optimal segmentation threshold by maximising inter-class variance. This method is effective for materials with bimodal intensity distributions, where pores and solid structures have distinct grayscale values[19,67,69].
- **Entropy-Based Thresholding**: The foreground and background are treated as separate sources and the optimal threshold is chosen at the maximum of the sum of the two class entropies. This is useful for images with complex histograms[24,27,45].
- **Histogram Thresholding**: Analysing the concavity points of the image's histograms convex hull. Any valley may be considered as potential threshold with the deepest concavities being favoured[27,70].

- **Local (Adaptive) Thresholding**: The threshold varies across different regions, allowing segmentation in images, in which contrast changes due to uneven illumination or varying material densities. This is useful for heterogenous structures[16,20,25,54,71]. Several local thresholding techniques exist as outlined by Rajagopalan et al.[27].
- **Contrast Enhancement with Fourier Transform**: Fourier-based contrast enhancement has been integrated to improve edge detection in biomaterial samples, particularly in scaffold imaging[5].
- **Manual Thresholding in ImageJ**: Adjusting the threshold manually to match original image features, as seen in some studies[1,72–76]. This technique can introduce various problems associated with room lighting, fatigue of the operator and limited grey-scale shade perception[27].
- **MATLAB-Optimised Thresholding:**
  - **Region-Growing and Edge-Detection Algorithms:** Allows for adaptive thresholding, enhancing pore segmentation in fibrous and highly interconnected structures[77,52].
  - **Gradient Filters:** Improve thresholding accuracy by refining intensity distributions, minimising over-segmentation errors[78,79]

- **Watershed-Based Segmentation:** The watershed algorithm is a region-based segmentation technique that treats an image as a topographic surface, where intensity variations correspond to elevations. It is useful for segmenting complex pore structures in porous materials by identifying watershed lines that separate adjacent regions. Following initial segmentation, the watershed algorithm refines pore boundaries by treating intensity gradients as a height map. By simulating the flooding of an image, it effectively separates adjacent pores that may have been grouped together in thresholding-based segmentation. While this method enhances segmentation accuracy, it may require post-processing to address over-segmentation[18,19,43,45,48,66,80]. MATLAB-based implementations of the watershed algorithm further improve pore segmentation accuracy through gradient-based seed point refinement[43].
  - **Gradient-Based Watershed:** Uses the gradient magnitude image to detect high-intensity ridges that define the segmented boundaries[24].
  - **Marker-Controlled Watershed:** Introduces predefined seed points to prevent over-segmentation, which is beneficial for fibrous or highly interconnected porous materials[20,66,43].

View Article Online
DOI: 10.1039/D5TB00848D

- **3D Watershed for Pore Connectivity:** Applied in voxel-based 3D reconstructions to quantify pore interconnectivity in porous scaffolds[18,19,43,66,48,81,80].

📌 Machine Learning-Based Pixel Classification

- **Shallow ML Models**: Shallow learners struggle to classify raw image input and depend on efficient preprocessing and predefined, representative characteristics such as intensity and edges.[27].
- **Deep Learning Models**: Deep learning models have demonstrated enhanced performance in segmenting irregular and disordered pore architectures, particularly in hydrogels and scaffolds[10,62,63]. CNNs and U-Net architectures learn hierarchical representations from large datasets, allowing robust segmentation of complex pore structures[5,20] . These model are capable to automatic feature selection and extraction, enhancing contrast in low-resolution porous material and removing the need for manual tuning[62]. Furthermore, advanced machine learning techniques improve segmentation across multiple imaging modalities, making them adaptable to various pore architectures[61]. One problem with deep learning models is their data hungry nature, requiring large, annotated datasets for successful training and prevention of overfitting.
  - **CNN-Based Approaches:** The convolutional nature of CNN's enables multi-scale feature extraction, which improves segmentation accuracy, enhances pore boundary detection and reduces errors in low-contrast regions[63]. The hierarchical nature of CNNs refines pore morphology, effectively distinguishing pores from material phases. Pretrained CNN models, such as VGG16 and ResNet, further accelerate adaptation by reducing the need for large, manually annotated training sets, while transfer learning enhances model generalisability across different biomaterial types, ensuring consistent segmentation accuracy[61,62].
  - **U-Net Architecture Approaches:** Provide pixel-wise segmentation, making them particularly effective for highly interconnected porous biomaterial. Their encoder-decoder structure allows for detailed feature extraction, while skip connections preserve fine-grained pore structures, significantly improving segmentation accuracy. Furthermore, data augmentation techniques enhance model robustness, compensating for limited training datasets and increasing adaptability across various biomaterial imaging conditions[5,61]

The following software given in Table 2 include modalities for different segmentation techniques. It is important to note that many studies utilise in-house, tailor-made code to conduct segmentation, that best befits their requirements.

Table 2. Examples of some readily available segmentation software.

Software	Built-In Segmentation
SPIP[82–84]	Intensity-based thresholding.
PoreSpy[85–88]	Watershed segmentation, deep-learning for pixel-wise classification.
Insight Toolkit (ITK)[80,89]	Otsu and binary thresholding, watershed segmentation.

View Article Online
DOI: 10.1039/D5TB00848D

Thermo Fisher Porometric Software[90]	Gradient-based and marker-controlled watershed methods for segmentation refinement.
MIPAR[42,91]	Multiple threshold, watershed and deep learning-based methods.
Mathematica[38,92,93]	Adaptive and histogram threshold, various watershed analyses.

Both threshold and machine learning-based approaches offer unique advantages to image segmentation with neither demonstrating consistently better performance albeit machine learning offers faster computation time. The choice of segmentation technique directly influences measures of porosity and pore structures, and the careful validation of image-based pore data remains crucial[45,64,94].

Figure 2: Examples of segmentation methods.
All images have been reproduced with permission.
A: 3D collagen network binarisation method. Left: Representative image cube of a 5(6)-Carboxytetramethylrhodamine N-succinimidylester (TAMRA)-labelled collagen scaffold. Right: A representative 2D slice of original image data, Otsu's thresholding, adaptive local thresholding of a denoised and the final segmentation result[16].
B: An unthresholded, undespeckled section of a micro-CT image of a collagen scaffold, demonstrating the noise which can be present in this type of data. Top right: Shows collagen in white, with the noise manually removed. Black represents void. Bottom right: shows the isolated noise, seen as light grey specks[57].
C: Overview of how the DiameterJ algorithm analyses fiber diameter and other scaffold properties[56].
D: Top left: CLSM images of nanomicrofiber scaffolds. Top right: filtered with median 3D. Bottom left: binarised. Bottom right: 3D reconstructed with Avizo Fire software[43].
E: Top: Binarised image of a PVA scaffold. Bottom: Separation of pores using the watershed algorithm[45].
F: Effect of pixel intensity threshold, K, on pore identification and resulting effect on pore size of scaffolds[3].

3.3 Pore Analysis: Techniques for Quantification

Once segmentation is complete, various pore analysis techniques are employed to quantify structural parameters such as pore size distribution, shape, and connectivity. Below, in Box 2, we examine some commonly used automated approaches of quantifying pore size. In addition, Table 3 provides an overview of some pore-analysis software packages and their respective capabilities with regard to pore size determination. While some software maybe more commonly used, others maybe at an emerging level. The outcome of analysis may differ depending on software choice (Figure 3).

Box 2: Pore Analysis Approaches

📌 Basic Metrics from Segmentation

View Article Online
DOI: 10.1039/D5TB00848D

- **Pore-to-Material Ratio**: The fraction of pore area relative to material area, expressed as a decimal or percentage. This is calculated using tools such as ImageJ or FiJi, which is useful for assessing porosity, however, lacks structural context[77,95,67,96,24,64] .
- **Pore Count**: The total number of detected pores; limited when pores are irregular or overlapping. Suited for homogenous structures.[5,21].
- **Pore Area Distribution**: Captures variability in pore sizes; however, segmentation errors can skew results[6,21,45,59,67,77].

📌 Advanced Pore Analysis Techniques

Pixel-Based Approaches

- **Exponential Decay Fit to Pore Pixel Spacing Distribution**: Quantifies the spatial arrangement of pores by fitting an exponential decay model to the pore-pixel spacing distribution[27]. This approach helps distinguish between homogeneous (evenly distributed pores) and heterogeneous (randomly distributed or clustered pores) porous networks.
- **Fourier Transform Analysis**: Used to detect periodicity in pore spacing, Fourier analysis can reveal structural anisotropy within porous scaffolds and hydrogels[71,36,77,97].
- **Skeletonisation-Based Analysis**: By reducing pore structures to their one-dimensional (1D) medial axis, this approach allows for measuring pore branching, interconnectivity, tortuosity and transport pathways in porous biomaterials scaffold[19,56,98,38].

Geometric Transform-Based Methods

- **Maximum Covering Radius Transform (CRT)**: The CRT method determines the largest inscribed circle within each pore, quantifying local pore size variations across a sample[55,46,66,99,100].
- **Morphological Opening and Closing Transformations**: These operations refine pore boundaries by removing small artifacts and enhancing true pore structures, aiding in more accurate segmentation[47,65,18,16,1,19,54,66]. For instance, connected pores can be separated using morphological dilation followed by erosion—dilation shrinks the pores by expanding scaffold boundaries, and erosion then restores pore size while maintaining separation[1].
- **Voxel-Based Pore Size Distribution (PSD) Reconstruction:** 3D voxel reconstruction has been used to quantify PSDs, for improved interconnectivity analysis[4,38,56,66,67].
- **Fourier-Based Feature Extraction for Pore Shape:** Fourier-based shape analysis has been integrated into voxel-based reconstructions to improve pore morphology quantification[5].

Pore Fitting Methods

- **Sphere/Circle Fitting**: Pore fitting methods are based on fitting a circle or a sphere to a pore, based on criteria such major diameter (MD, major diameter of analysed pore), mean thickness (MT, based on circle-fitting algorithm similar to sphere-fitting method), biggest inner circle diameter (BICD, diameter of the biggest circle

View Article Online
DOI: 10.1039/D5TB00848D

that fits the pore) and area-equivalent circle diameter (AECD, diameter of the circle with an equivalent area to that of the pore) [12,46,65,66,48,67,99,101,97,45]. Ideally well suited for circular pores[1].

- **Bubble Analysis**: Bubble analysis is a geometric method that mimics fluid dynamics in fibrous networks and is based on the largest possible circle inside a pore that touches three surrounding fibers[16,17,46,53], however, according to Fischer et al. may not fully account for the residual fluid volume[16]. In an article-response dynamic, Molteni et al. proposed an algorithm that randomly seeds a pore and expands its boundary until it tangentially contacts three fibers[17], for which Münster & Fabry developed a simplified approach using Euclidean distance mapping to detect local maxima, identifying the largest pore regions[102]. However, Molteni et al. argued that this method lacks filtering and requires additional post-processing to remove overlapping pores and those that do not satisfy the three-fiber contact criterion[103]. Applicable to fibrous networks such as bundled F-actin, fibrin, cytoskeletal filament networks, given individual fibers can be resolved[53].
- **Destroy and Rebuild Method for PSD Analysis:**
  This micro-CT-based technique reconstructs 3D pore networks from 2D slice data, offering an alternative to direct segmentation-based methods. ImageJ's particle analyser (PA) function extracts mass centre coordinates (Xc, Yc) and pore section areas for each binarised slice. An algorithm groups sections by spatial proximity, assuming pores maintain a spherical shape. Edge-affected pores are removed, and equivalent volume and radius are calculated for each pore to determine the PSD[5,45,56] In addition, MATLAB-based PSD reconstruction methods have been applied to improve accuracy in volume estimations of irregularly shaped pores[77].

Table 3. Examples of commonly used pore-analysis software.

Software	Built-In Analysis
SPIP[82–84]	1. Pore size distribution 2. Interconnectivity, and transport pathways 3. Quantification using geometric fitting methods 4. Skeletonisation 5. Voxel-based analysis
MIPAR[42,91]	
Sigma Scan Pro 5[96,104]	
Materialise Mimics[65]	
CTAn (Bruker) [46,105,106]	
Quanfima[24]	
Image-Pro Plus[107–110]	
[79–82]	Enhances pore network characterisation with skeletonisation-based metrics.
GeoDict[44]	CRT and micro-CT-based PSD reconstruction.
Amira (TGS, San Diego, CA)[19,111]	Skeletonisation.
ImageJ Plugin DiameterJ[24,41,56]	Measure porosity of fibre networks.
ImageJ Plugins ND[112]	Measure porosity of scaffolds.
ImageJ – Plugins BoneJ[56,99]	Measure porosity of bone structures.
PoreVision[20]	Pore size analysis including measurement, distribution and range. Morphological analysis.

View Article Online
DOI: 10.1039/D5TB00848D

Figure 3: Examples of automated pore size determination methods.
All images have been reproduced with permission.
A: Quantification of 3D pore networks of sol–gel derived bioactive glass foams from micro-CT data: (a) 2D slice of raw data, (b) 2D slice showing application of the dilation algorithm, (c) 2D representation of pores derived from the watershed algorithm, (d) 3D image of identified pores, (e) 3D image of the interconnects obtained from the top down algorithm, and (f) demonstration of the bounding box method of measuring the interconnect length[19].
B: Illustration of pore size determination of alginate hydrogel microcapsules using TEM images. Image A depicts a hydrogel as it is typically observed using transmission electron microscopy. Image B shows the results of the image segmentation after binarisation. Image C shows the result of a Euclidean distance transformation. Image D gives an overlay of the pore region image skeleton (red lines) with the original image. Image skeletons are one-pixel wide center axes. They are defined via the set of inner pore pixels. The set is defined via local distance maxima with respect to alginate segments[38].
C: Fiber network diameter determination of scaffolds (opposite of pore size determination, using similar algorithms). Top left: starting SEM image. Top centre: image histogram equalsation followed by 3 by 3 median filtering. Top right: local thresholding through Otsu method. Middle left: thinning, smoothing and removal of isolated pixel areas through a cascade of different morphological operators. Middle center: skeletonization. Middle right – Bottom left: binary filters for Delaunay network refinement. Bottom center: modified Delaunay network associated to the real fiber network. Bottom right: final network and fiber diameters detected[25].
D: Simplified bubble analysis of the pore space of a random biopolymer network in two steps. Left: first, the Euclidean distance map (EDM) of the fluid space of the network structure is computed (shades of gray (colours online) indicate the distance of each fluid pixel to the nearest fiber pixel). (Black) Fibers. Second, the local maxima of the EDM (white crosses) determine the centres of all 2D bubbles. To avoid bubbles of similar size in close proximity, the EDM was smoothed with a 5 × 5 Gaussian kernel with a sigma of one before the local maxima were determined. (Inset) A local maximum of the EDM (red circle) is a pixel whose eight neighbours all have smaller values. Right: Resulting 2D bubbles (black circles) fit into the pore zones of the fiber structure (black). (Red crosses) Bubble centers[102].
E: Comparison of detected pores with cutoff values of 85 vs. 120 in Chitosan-gelatin cryogels using PoreVision software. Red outlines are pores outside the analysis boundary, blue outlines are pores removed for being too small (most likely dust, cracks, or folds), and green outlines are identified pores[20].
F: Illustration of varying results provided by micro-CT 2D pore size analysis of collagen-based scaffolds. Pores (in gray) of 3 differing shapes (left, centre, right) were evaluated by means of 4 micro-CT 2D parameters (MT—mean thickness, MD—major diameter, BICD—biggest inner circle diameter, AECD—area-equivalent circle diameter) and their values are presented in panels below the images (in mm). The results tend to differ with increasing shape irregularity[46].
G: Colour map and pixel intensity based measurement of macro pore size distribution in a polymeric scaffold[21].

4. Summary, Recommendations and Future Directions

Automated pore size analysis in biomaterials remains a field of active development, with several challenges and opportunities ahead. A persistent issue is the control of measurement

View Article Online
DOI: 10.1039/D5TB00848D

error, which can arise at multiple stages of the workflow, from image acquisition to segmentation and feature extraction, ultimately affecting data reliability.

Imaging quality—including resolution, magnification, and field of view—strongly influences the accuracy of segmentation and measurement methods. Poor image quality or insufficient resolution often leads to inconsistent or inaccurate pore size detection, particularly in fibrous or highly irregular networks[41,47].

Circle-fitting algorithms can be useful for regular, isotropic materials with well-defined, circular pores, but often over- or underestimate pore sizes in more complex biomaterials. Many image analysis tools still depend on manual thresholding, subjective filtering, or operator bias, particularly when the software allows for interactive selection or exclusion of pores during post-processing[20]. While software such as DiameterJ and PoreSpy offer user-friendly platforms, their results are sensitive to image parameters, such as pixel size and contrast depth, and sometimes require subjective validation[41].

Importantly, there is no universal standard or pipeline for PSD analysis that suits all materials. Algorithms often need to be tailored to specific scaffold morphologies. Nevertheless, some methods demonstrate cross-material applicability, successfully analysing electrospun meshes, hydrogels, and decellularised tissues with the same underlying algorithm[25].

A growing concern in the literature is the lack of detailed reporting on how PSD is computed. Some studies present PSD values without any or very limited mention of segmentation methods, threshold settings, or image pre-processing steps, and many studies cite ‘in-house algorithms’ without sufficient detail or provided code[18,20,24,41]. This hampers reproducibility and impedes method comparison while inconsistency in terminology increases the entry barrier to the field. Moreover, claims of “fully automated” analysis often mask semi-automated steps that introduce bias, such as filtering out overlapping or irregular pores without objective criteria[41]. Closely related to this is the inconsistency across reported metrics, with many studies failing to report objective evaluations of the PSD methodology.

Most current approaches rely on unsupervised learning methods without a reference standard or ‘ground-truth’, which makes performance evaluation difficult. Many studies rely on qualitative validation (visual matching) rather than reporting consistent quantitative metrics such as measurement error or precision. When validation is provided, it is often inconsistent or non-comparable across studies[20]. This may be partially attributed to the lack of available ‘ground-truth’ values, which makes the implementation of supervised learning challenging. However, while the manual measurement of pore size is difficult and includes human error, studies should aim to validate proposed automated methods using ‘ground-truth’ measurements to ascertain the reliability of the selected methods.

Closely related is a need for reporting objective evaluation metrics of automated methods. While the lack of ‘ground-truth’ complicates the implementation of supervised learning, steps should be taken to evaluate algorithms in the absence of a ‘true’ value. While some studies have implemented algorithm validation using standard reference images[1], others compare results between methods to establish mean performance and improve reliability of findings. While several supervised and unsupervised evaluation methods thus exist, many studies continue to accept pore size estimation at face value without considering the associated bias of the measurement tool. Future studies should aim to conduct critical evaluation of their

View Article Online
DOI: 10.1039/D5TB00848D

estimation techniques and in the absence of an objective 'ground-truth' should at the very least compare the performances of different algorithms.

There is also limited ability among automated algorithms to handle irregularly shaped or anisotropic pores. Many algorithms interpret elongated or eccentric pores as two or more circular pores, which misrepresents the actual pore size distribution[35]. While some algorithms have introduced shape classification features, their accuracy for small or faint shapes remains limited.

Looking ahead, a promising direction is the integration of machine learning and deep learning approaches trained on annotated datasets to improve pore recognition and classification accuracy. This includes the potential for algorithms that are not only shape-aware but also context-aware—able to distinguish between artefacts and true pores based on their position, orientation, or relationship with surrounding structures.

We recommend the following:

- **Standardised Reporting**: All studies should include detailed information on segmentation algorithms, image processing steps, and evaluation metrics used in PSD analysis.
- **Material-Specific Validation**: Algorithms should be validated for specific scaffold types and pore morphologies, not assumed to be generalisable.
- **Open-Source Development**: Wider adoption of open-source platforms would promote reproducibility, comparability, and collaborative development.
- **Integration of AI and ML**: Supervised machine learning and AI-enhanced approaches could overcome current limitations in pore shape recognition, classification, and error quantification.
- **Consistency in Evaluation**: Future studies should report standard error metrics and comparison benchmarks to assess accuracy, ideally using both synthetic and real-world datasets.

Ultimately, while automated PSD analysis is advancing rapidly, further work is needed to balance ease of use, reproducibility, and the ability to capture complex pore features across diverse biomaterials, including dynamic hydrogels and 4D scaffolds.

Conflicts of Interest

The authors declare no conflicts of interest.

Data Availability Statement

No primary research results, software or code have been included and no new data were generated or analysed as part of this perspective.

Author Contributions

IJ led the drafting of the manuscript, prepared the figures, and served as the corresponding author. IJ, LG, and SC provided expertise and oversight on the biomaterials-related

View Article Online
DOI: 10.1039/D5TB00848D

components of the work, while NR and SC contributed guidance on the automated analysis and computational aspects. IJ primarily compiled sections focused on biomaterials, and NR focused on the sections related to automated image analysis techniques. All authors contributed to the editing and final approval of the manuscript.

Acknowledgments

The authors acknowledge helpful suggestions from Dr Petri Turunen. IJ acknowledges funding support from Marie Skłodowska-Curie Actions (MSCA) and Research Ireland-Grant Number: 847652. This publication has emanated from research conducted with the financial support of Taighde Éireann - Research Ireland under Grant No. 18/CRT/6223 (NR). Finally, the TOC image was created with BioRender.com.

References

(1) Hojat, N.; Gentile, P.; Ferreira, A. M.; Šiller, L. Automatic Pore Size Measurements from Scanning Electron Microscopy Images of Porous Scaffolds. *J. Porous Mater.* **2023**, *30* (1), 93–101. https://doi.org/10.1007/s10934-022-01309-y.

(2) Jayawardena, I.; Turunen, P.; Garms, B. C.; Rowan, A.; Corrie, S.; Grøndahl, L. Evaluation of Techniques Used for Visualisation of Hydrogel Morphology and Determination of Pore Size Distributions. *Mater Adv* **2023**, *4* (2), 669–682. https://doi.org/10.1039/D2MA00932C.

(3) Jenkins, D.; Salhadar, K.; Ashby, G.; Mishra, A.; Cheshire, J.; Beltran, F.; Grunlan, M.; Andrieux, S.; Stubenrauch, C.; Cosgriff-Hernandez, E. PoreScript: Semi-Automated Pore Size Algorithm for Scaffold Characterization. *Bioact. Mater.* **2022**, *13*, 1–8. https://doi.org/10.1016/j.bioactmat.2021.11.006.

(4) Van Cleynenbreugel, T.; Schrooten, J.; Van Oosterwyck, H.; Vander Sloten, J. Micro-CT-Based Screening of Biomechanical and Structural Properties of Bone Tissue Engineering Scaffolds. *Med. Biol. Eng. Comput.* **2006**, *44* (7), 517–525. https://doi.org/10.1007/s11517-006-0071-z.

(5) Karaca, I.; Aldemir Dikici, B. Quantitative Evaluation of the Pore and Window Sizes of Tissue Engineering Scaffolds on Scanning Electron Microscope Images Using Deep Learning. *ACS Omega* **2024**, *9* (23), 24695–24706. https://doi.org/10.1021/acsomega.4c01234.

(6) Singh, Y. P.; Bhardwaj, N.; Mandal, B. B. Potential of Agarose/Silk Fibroin Blended Hydrogel for in Vitro Cartilage Tissue Engineering. *ACS Appl. Mater. Interfaces* **2016**, *8* (33), 21236–21249. https://doi.org/10.1021/acsami.6b08285.

(7) Solbu, A. A.; Caballero, D.; Damigos, S.; Kundu, S. C.; Reis, R. L.; Halaas, Ø.; Chahal, A. S.; Strand, B. L. Assessing Cell Migration in Hydrogels: An Overview of Relevant Materials and Methods. *Mater. Today Bio* **2023**, *18*, 100537. https://doi.org/10.1016/j.mtbio.2022.100537.

(8) Stachewicz, U.; Szewczyk, P. K.; Kruk, A.; Barber, A. H.; Czyrska-Filemonowicz, A. Pore Shape and Size Dependence on Cell Growth into Electrospun Fiber Scaffolds for Tissue Engineering: 2D and 3D Analyses Using SEM and FIB-SEM Tomography. *Mater. Sci. Eng. C* **2019**, *95*, 397–408. https://doi.org/10.1016/j.msec.2017.08.076.

(9) Bryant, S. J.; Cuy, J. L.; Hauch, K. D.; Ratner, B. D. Photo-Patterning of Porous Hydrogels for Tissue Engineering. *Biomaterials* **2007**, *28* (19), 2978–2986. https://doi.org/10.1016/j.biomaterials.2006.11.033.

View Article Online
DOI: 10.1039/D5TB00848D

(10) Negut, I.; Bita, B. Exploring the Potential of Artificial Intelligence for Hydrogel Development—A Short Review. *Gels* **2023**, *9* (11). https://doi.org/10.3390/gels9110845.
(11) Appleyard, D. C.; Chapin, S. C.; Srinivas, R. L.; Doyle, P. S. Bar-Coded Hydrogel Microparticles for Protein Detection: Synthesis, Assay and Scanning. *Nat. Protoc.* **2011**, *6* (11), 1761–1774. https://doi.org/10.1038/nprot.2011.400.
(12) Cameron, A. P.; Zeng, B.; Liu, Y.; Wang, H.; Soheilmoghaddam, F.; Cooper-White, J.; Zhao, C.-X. Biophysical Properties of Hydrogels for Mimicking Tumor Extracellular Matrix. *Biomater. Adv.* **2022**, *136*, 212782. https://doi.org/10.1016/j.bioadv.2022.212782.
(13) Kaufman, L. J.; Brangwynne, C. P.; Kasza, K. E.; Filippidi, E.; Gordon, V. D.; Deisboeck, T. S.; Weitz, D. A. Glioma Expansion in Collagen I Matrices: Analyzing Collagen Concentration-Dependent Growth and Motility Patterns. *Biophys. J.* **2005**, *89* (1), 635–650. https://doi.org/10.1529/biophysj.105.061994.
(14) Kuntz, R. M.; Saltzman, W. M. Neutrophil Motility in Extracellular Matrix Gels: Mesh Size and Adhesion Affect Speed of Migration. *Biophys. J.* **1997**, *72* (3), 1472–1480. https://doi.org/10.1016/S0006-3495(97)78793-9.
(15) Domingos, M.; Intranuovo, F.; Russo, T.; Santis, R. D.; Gloria, A.; Ambrosio, L.; Ciurana, J.; Bartolo, P. The First Systematic Analysis of 3D Rapid Prototyped Poly(ε-Caprolactone) Scaffolds Manufactured through BioCell Printing: The Effect of Pore Size and Geometry on Compressive Mechanical Behaviour and in Vitro hMSC Viability. *Biofabrication* **2013**, *5* (4), 045004. https://doi.org/10.1088/1758-5082/5/4/045004.
(16) Fischer, T.; Hayn, A.; Mierke, C. T. Fast and Reliable Advanced Two-Step Pore-Size Analysis of Biomimetic 3D Extracellular Matrix Scaffolds. *Sci. Rep.* **2019**, *9* (1), 8352. https://doi.org/10.1038/s41598-019-44764-5.
(17) Molteni, M.; Magatti, D.; Cardinali, B.; Rocco, M.; Ferri, F. Fast Two-Dimensional Bubble Analysis of Biopolymer Filamentous Networks Pore Size from Confocal Microscopy Thin Data Stacks. *Biophys. J.* **2013**, *104* (5), 1160–1169. https://doi.org/10.1016/j.bpj.2013.01.016.
(18) Atwood, R. C.; Jones, J. R.; Lee, P. D.; Hench, L. L. Analysis of Pore Interconnectivity in Bioactive Glass Foams Using X-Ray Microtomography. *Scr. Mater.* **2004**, *51* (11), 1029–1033. https://doi.org/10.1016/j.scriptamat.2004.08.014.
(19) Jones, J. R.; Poologasundarampillai, G.; Atwood, R. C.; Bernard, D.; Lee, P. D. Non-Destructive Quantitative 3D Analysis for the Optimisation of Tissue Scaffolds. *Biomaterials* **2007**, *28* (7), 1404–1413. https://doi.org/10.1016/j.biomaterials.2006.11.014.
(20) Olevsky, L. M.; Jacques, M. G.; Hixon, K. R. PoreVision: A Program for Enhancing Efficiency and Accuracy in SEM Pore Analyses of Gels and Other Porous Materials. *Gels* **2025**, *11* (2). https://doi.org/10.3390/gels11020132.
(21) Re, G. L.; Lopresti, F.; Petrucci, G.; Scaffaro, R. A Facile Method to Determine Pore Size Distribution in Porous Scaffold by Using Image Processing. *Micron* **2015**, *76*, 37–45. https://doi.org/10.1016/j.micron.2015.05.001.
(22) Thu, K.; Chakraborty, A.; Saha, B. B.; Ng, K. C. Thermo-Physical Properties of Silica Gel for Adsorption Desalination Cycle. *Appl. Therm. Eng.* **2013**, *50* (2), 1596–1602. https://doi.org/10.1016/j.applthermaleng.2011.09.038.
(23) The Quest for Quantitative Microscopy. *Nat. Methods* **2012**, *9* (7), 627–627. https://doi.org/10.1038/nmeth.2102.
(24) Shkarin, R.; Shkarin, A.; Shkarina, S.; Cecilia, A.; Surmenev, R. A.; Surmeneva, M. A.; Weinhardt, V.; Baumbach, T.; Mikut, R. Quanfima: An Open Source Python Package

View Article Online
DOI: 10.1039/D5TB00848D

for Automated Fiber Analysis of Biomaterials. *PLOS ONE* **2019**, *14* (4), 1–20. https://doi.org/10.1371/journal.pone.0215137.

(25) D'Amore, A.; Stella, J. A.; Wagner, W. R.; Sacks, M. S. Characterization of the Complete Fiber Network Topology of Planar Fibrous Tissues and Scaffolds. *Biomaterials* **2010**, *31* (20), 5345–5354. https://doi.org/10.1016/j.biomaterials.2010.03.052.

(26) Chen, C.-W.; Betz, M. W.; Fisher, J. P.; Paek, A.; Chen, Y. Macroporous Hydrogel Scaffolds and Their Characterization By Optical Coherence Tomography. *Tissue Eng. Part C Methods* **2011**, *17* (1), 101–112. https://doi.org/10.1089/ten.tec.2010.0072.

(27) Rajagopalan, S.; Lu, L.; Yaszemski, M. J.; Robb, R. A. Optimal Segmentation of Microcomputed Tomographic Images of Porous Tissue-Engineering Scaffolds. *J. Biomed. Mater. Res. A* **2005**, *75A* (4), 877–887. https://doi.org/10.1002/jbm.a.30498.

(28) Richbourg, N. R.; Ravikumar, A.; Peppas, N. A. Solute Transport Dependence on 3D Geometry of Hydrogel Networks. *Macromol. Chem. Phys.* **2021**, *222* (16), 2100138.

(29) First, E. L.; Floudas, C. A. MOFomics: Computational Pore Characterization of Metal–Organic Frameworks. *Microporous Mesoporous Mater.* **2013**, *165*, 32–39. https://doi.org/10.1016/j.micromeso.2012.07.049.

(30) Miklitz, M.; Jelfs, K. E. Pywindow: Automated Structural Analysis of Molecular Pores. *J. Chem. Inf. Model.* **2018**, *58* (12), 2387–2391. https://doi.org/10.1021/acs.jcim.8b00490.

(31) Trepte, K.; Schwalbe, S. porE: A Code for Deterministic and Systematic Analyses of Porosities. *J. Comput. Chem.* **2021**, *42* (9), 630–643. https://doi.org/10.1002/jcc.26484.

(32) First, E. L.; Gounaris, C. E.; Wei, J.; Floudas, C. A. Computational Characterization of Zeolite Porous Networks: An Automated Approach. *Phys Chem Chem Phys* **2011**, *13* (38), 17339–17358. https://doi.org/10.1039/C1CP21731C.

(33) Willems, T. F.; Rycroft, C. H.; Kazi, M.; Meza, J. C.; Haranczyk, M. Algorithms and Tools for High-Throughput Geometry-Based Analysis of Crystalline Porous Materials. *Microporous Mesoporous Mater.* **2012**, *149* (1), 134–141. https://doi.org/10.1016/j.micromeso.2011.08.020.

(34) Pinheiro, M.; Martin, R. L.; Rycroft, C. H.; Jones, A.; Iglesia, E.; Haranczyk, M. Characterization and Comparison of Pore Landscapes in Crystalline Porous Materials. *J. Mol. Graph. Model.* **2013**, *44*, 208–219. https://doi.org/10.1016/j.jmgm.2013.05.007.

(35) Kim, H. Y.; Maruta, R. H.; Huanca, D. R.; Salcedo, W. J. Correlation-Based Multi-Shape Granulometry with Application in Porous Silicon Nanomaterial Characterization. *J. Porous Mater.* **2013**, *20* (2), 375–385. https://doi.org/10.1007/s10934-012-9607-9.

(36) Oviatt, H. W. Jr.; Shea, K. J.; Small, J. H. Alkylene-Bridged Silsesquioxane Sol-Gel Synthesis and Xerogel Characterization. Molecular Requirements for Porosity. *Chem. Mater.* **1993**, *5* (7), 943–950. https://doi.org/10.1021/cm00031a012.

(37) Gupta, D.; Venugopal, J.; Mitra, S.; Dev, V. R. G.; Ramakrishna, S. Nanostructured Biocomposite Substrates by Electrospinning and Electrospraying for the Mineralization of Osteoblasts. *Biomaterials* **2009**, *30* (11), 2085–2094. https://doi.org/10.1016/j.biomaterials.2008.12.079.

(38) Leal-Egaña, A.; Braumann, U.-D.; Díaz-Cuenca, A.; Nowicki, M.; Bader, A. Determination of Pore Size Distribution at the Cell-Hydrogel Interface. *J. Nanobiotechnology* **2011**, *9* (1), 24. https://doi.org/10.1186/1477-3155-9-24.

(39) Krauss, P.; Metzner, C.; Lange, J.; Lang, N.; Fabry, B. Parameter-Free Binarization and Skeletonization of Fiber Networks from Confocal Image Stacks. *PLOS ONE* **2012**, *7* (5), 1–8. https://doi.org/10.1371/journal.pone.0036575.

(40) Wolf, M. T.; Daly, K. A.; Brennan-Pierce, E. P.; Johnson, S. A.; Carruthers, C. A.; D'Amore, A.; Nagarkar, S. P.; Velankar, S. S.; Badylak, S. F. A Hydrogel Derived from

Decellularized Dermal Extracellular Matrix. *Biomaterials* **2012**, *33* (29), 7028–7038. https://doi.org/10.1016/j.biomaterials.2012.06.051.

(41) Daraei, A.; Pieters, M.; Baker, S. R.; de Lange-Loots, Z.; Siniarski, A.; Litvinov, R. I.; Veen, C. S. B.; de Maat, M. P. M.; Weisel, J. W.; Ariëns, R. A. S.; Guthold, M. Automated Fiber Diameter and Porosity Measurements of Plasma Clots in Scanning Electron Microscopy Images. *Biomolecules* **2021**, *11* (10). https://doi.org/10.3390/biom11101536.

(42) Kheradvar Kolour, A.; Ghoraishizadeh, S.; Zaman, M. S.; Alemzade, A.; Banavand, M.; Esmaeili, J.; Shahrousvand, M. Janus Films Wound Dressing Comprising Electrospun Gelatin/PCL Nanofibers and Gelatin/Honey/Curcumin Thawed Layer. *ACS Appl. Bio Mater.* **2024**, *7* (12), 8642–8655. https://doi.org/10.1021/acsabm.4c01449.

(43) Bagherzadeh, R.; Latifi, M.; Najar, S. S.; Tehran, M. A.; Kong, L. Three-Dimensional Pore Structure Analysis of Nano/Microfibrous Scaffolds Using Confocal Laser Scanning Microscopy. *J. Biomed. Mater. Res. A* **2013**, *101A* (3), 765–774. https://doi.org/10.1002/jbm.a.34379.

(44) Schäfer, B.; Emonts, C.; Glimpel, N.; Ruhl, T.; Obrecht, A. S.; Jockenhoevel, S.; Gries, T.; Beier, J. P.; Blaeser, A. Warp-Knitted Spacer Fabrics: A Versatile Platform to Generate Fiber-Reinforced Hydrogels for 3D Tissue Engineering. *Materials* **2020**, *13* (16). https://doi.org/10.3390/ma13163518.

(45) Colosi, C.; Costantini, M.; Barbetta, A.; Pecci, R.; Bedini, R.; Dentini, M. Morphological Comparison of PVA Scaffolds Obtained by Gas Foaming and Microfluidic Foaming Techniques. *Langmuir* **2013**, *29* (1), 82–91. https://doi.org/10.1021/la303788z.

(46) Bartoš, M.; Suchý, T.; Foltán, R. Note on the Use of Different Approaches to Determine the Pore Sizes of Tissue Engineering Scaffolds: What Do We Measure? *Biomed. Eng. OnLine* **2018**, *17* (1), 110. https://doi.org/10.1186/s12938-018-0543-z.

(47) Franke, K.; Sapudom, J.; Kalbitzer, L.; Anderegg, U.; Pompe, T. Topologically Defined Composites of Collagen Types I and V as in Vitro Cell Culture Scaffolds. *Acta Biomater.* **2014**, *10* (6), 2693–2702. https://doi.org/10.1016/j.actbio.2014.02.036.

(48) Yue, S.; Lee, P. D.; Poologasundarampillai, G.; Yao, Z.; Rockett, P.; Devlin, A. H.; Mitchell, C. A.; Konerding, M. A.; Jones, J. R. Synchrotron X-Ray Microtomography for Assessment of Bone Tissue Scaffolds. *J. Mater. Sci. Mater. Med.* **2010**, *21* (3), 847–853. https://doi.org/10.1007/s10856-009-3888-9.

(49) Ma, T. M.; VanEpps, J. S.; Solomon, M. J. Structure, Mechanics, and Instability of Fibrin Clot Infected with Staphylococcus Epidermidis. *Biophys. J.* **2017**, *113* (9), 2100–2109. https://doi.org/10.1016/j.bpj.2017.09.001.

(50) ElHadidy, A. M.; Peldszus, S.; Dyke, M. I. V. Development of a Pore Construction Data Analysis Technique for Investigating Pore Size Distribution of Ultrafiltration Membranes by Atomic Force Microscopy. *J. Membr. Sci.* **2013**, *429*, 373–383. https://doi.org/10.1016/j.memsci.2012.11.054.

(51) Sundaramoorthi, G.; Hadwiger, M.; Ben-Romdhane, M.; Behzad, A. R.; Madhavan, P.; Nunes, S. P. 3D Membrane Imaging and Porosity Visualization. *Ind. Eng. Chem. Res.* **2016**, *55* (12), 3689–3695. https://doi.org/10.1021/acs.iecr.6b00387.

(52) Guarino, V.; Guaccio, A.; Netti, P. A.; Ambrosio, L. Image Processing and Fractal Box Counting: User-Assisted Method for Multi-Scale Porous Scaffold Characterization. *J. Mater. Sci. Mater. Med.* **2010**, *21* (12), 3109–3118. https://doi.org/10.1007/s10856-010-4163-9.

(53) Mickel, W.; Münster, S.; Jawerth, L. M.; Vader, D. A.; Weitz, D. A.; Sheppard, A. P.; Mecke, K.; Fabry, B.; Schröder-Turk, G. E. Robust Pore Size Analysis of Filamentous

Networks from Three-Dimensional Confocal Microscopy. *Biophys. J.* **2008**, *95* (12), 6072–6080. https://doi.org/10.1529/biophysj.108.135939.

(54) Wang, L.; Xu, M.; Zhang, L.; Zhou, Q.; Luo, L. Automated Quantitative Assessment of Three-Dimensional Bioprinted Hydrogel Scaffolds Using Optical Coherence Tomography. *Biomed Opt Express* **2016**, *7* (3), 894–910. https://doi.org/10.1364/BOE.7.000894.

(55) Lawrence, M.; Jiang, Y. Porosity, Pore Size Distribution, Micro-Structure. In *Bio-aggregates Based Building Materials : State-of-the-Art Report of the RILEM Technical Committee 236-BBM*; Amziane, S., Collet, F., Eds.; Springer Netherlands: Dordrecht, 2017; pp 39–71. https://doi.org/10.1007/978-94-024-1031-0_2.

(56) Hotaling, N. A.; Bharti, K.; Kriel, H.; Simon, C. G. DiameterJ: A Validated Open Source Nanofiber Diameter Measurement Tool. *Biomaterials* **2015**, *61*, 327–338. https://doi.org/10.1016/j.biomaterials.2015.05.015.

(57) Meek, M. C.; Best, S.; Cameron, R. The Effects of Despeckling Filters on Pore Size Measurements in Collagen Scaffold Micro-CT Data. *J. Microsc.* **2021**, *284* (2), 142–156. https://doi.org/10.1111/jmi.13050.

(58) Suh, H. S.; Song, J. Y.; Kim, Y.; Yu, X.; Choo, J. Data-Driven Discovery of Interpretable Water Retention Models for Deformable Porous Media. *Acta Geotech.* **2024**, *19* (6), 3821–3835. https://doi.org/10.1007/s11440-024-02322-y.

(59) Misra, S.; Wu, Y. Chapter 10 - Machine Learning Assisted Segmentation of Scanning Electron Microscopy Images of Organic-Rich Shales with Feature Extraction and Feature Ranking. In *Machine Learning for Subsurface Characterization*; Misra, S., Li, H., He, J., Eds.; Gulf Professional Publishing, 2020; pp 289–314. https://doi.org/10.1016/B978-0-12-817736-5.00010-7.

(60) Kalaiselvi, T.; Sriramakrishnan, P.; Somasundaram, K. Survey of Using GPU CUDA Programming Model in Medical Image Analysis. *Inform. Med. Unlocked* **2017**, *9*, 133–144. https://doi.org/10.1016/j.imu.2017.08.001.

(61) Perera, R.; Guzzetti, D.; Agrawal, V. Optimized and Autonomous Machine Learning Framework for Characterizing Pores, Particles, Grains and Grain Boundaries in Microstructural Images. *Comput. Mater. Sci.* **2021**, *196*, 110524. https://doi.org/10.1016/j.commatsci.2021.110524.

(62) LeCun, Y.; Bengio, Y.; Hinton, G. Deep Learning. *Nature* **2015**, *521* (7553), 436–444. https://doi.org/10.1038/nature14539.

(63) Ravì, D.; Wong, C.; Deligianni, F.; Berthelot, M.; Andreu-Perez, J.; Lo, B.; Yang, G.-Z. Deep Learning for Health Informatics. *IEEE J. Biomed. Health Inform.* **2017**, *21* (1), 4–21. https://doi.org/10.1109/JBHI.2016.2636665.

(64) Soliman, S.; Pagliari, S.; Rinaldi, A.; Forte, G.; Fiaccavento, R.; Pagliari, F.; Franzese, O.; Minieri, M.; Nardo, P. D.; Licoccia, S.; Traversa, E. Multiscale Three-Dimensional Scaffolds for Soft Tissue Engineering via Multimodal Electrospinning. *Acta Biomater.* **2010**, *6* (4), 1227–1237. https://doi.org/10.1016/j.actbio.2009.10.051.

(65) Lacroix, D.; Chateau, A.; Ginebra, M.-P.; Planell, J. A. Micro-Finite Element Models of Bone Tissue-Engineering Scaffolds. *Biomaterials* **2006**, *27* (30), 5326–5334. https://doi.org/10.1016/j.biomaterials.2006.06.009.

(66) Yue, S.; Lee, P. D.; Poologasundarampillai, G.; Jones, J. R. Evaluation of 3-D Bioactive Glass Scaffolds Dissolution in a Perfusion Flow System with X-Ray Microtomography. *Acta Biomater.* **2011**, *7* (6), 2637–2643. https://doi.org/10.1016/j.actbio.2011.02.009.

(67) Gorguluarslan, R. M.; Choi, S.-K.; Saldana, C. J. Uncertainty Quantification and Validation of 3D Lattice Scaffolds for Computer-Aided Biomedical Applications. *J. Mech. Behav. Biomed. Mater.* **2017**, *71*, 428–440. https://doi.org/10.1016/j.jmbbm.2017.04.011.

View Article Online
DOI: 10.1039/D5TB00848D

(68) Rezaei, F.; Izadi, H.; Memarian, H.; Baniassadi, M. The Effectiveness of Different Thresholding Techniques in Segmenting Micro CT Images of Porous Carbonates to Estimate Porosity. *J. Pet. Sci. Eng.* **2019**, *177*, 518–527. https://doi.org/10.1016/j.petrol.2018.12.063.
(69) Otsu, N. A. Threshold Selection Method from Gray-Level Histograms, lEE. *Trans Syst Man Cybern19799162* **1979**.
(70) Münch, B.; Holzer, L. Contradicting Geometrical Concepts in Pore Size Analysis Attained with Electron Microscopy and Mercury Intrusion. *J. Am. Ceram. Soc.* **2008**, *91* (12), 4059–4067. https://doi.org/10.1111/j.1551-2916.2008.02736.x.
(71) Bayan, C.; Levitt, J. M.; Miller, E.; Kaplan, D.; Georgakoudi, I. Fully Automated, Quantitative, Noninvasive Assessment of Collagen Fiber Content and Organization in Thick Collagen Gels. *J. Appl. Phys.* **2009**, *105* (10), 102042. https://doi.org/10.1063/1.3116626.
(72) Lin, A. S. P.; Barrows, T. H.; Cartmell, S. H.; Guldberg, R. E. Microarchitectural and Mechanical Characterization of Oriented Porous Polymer Scaffolds. *Biomaterials* **2003**, *24* (3), 481–489. https://doi.org/10.1016/S0142-9612(02)00361-7.
(73) Filmon, R.; Retailleau-Gaborit, N.; Grizon, F.; Galloyer, M.; Cincu, C.; Basle, M. F.; and, D. C. Non-Connected versus Interconnected Macroporosity in Poly(2-Hydroxyethyl Methacrylate) Polymers. An X-Ray Microtomographic and Histomorphometric Study. *J. Biomater. Sci. Polym. Ed.* **2002**, *13* (10), 1105–1117. https://doi.org/10.1163/156856202320813828.
(74) Elmoutaouakkil, A.; Fuchs, G.; Bergounhon, P.; Péres, R.; Peyrin, F. Three-Dimensional Quantitative Analysis of Polymer Foams from Synchrotron Radiation x-Ray Microtomography. *J. Phys. Appl. Phys.* **2003**, *36* (10A), A37. https://doi.org/10.1088/0022-3727/36/10A/308.
(75) Itoh, M.; Shimazu, A.; Hirata, I.; Yoshida, Y.; Shintani, H.; Okazaki, M. Characterization of CO3Ap-Collagen Sponges Using X-Ray High-Resolution Microtomography. *Biomaterials* **2004**, *25* (13), 2577–2583. https://doi.org/10.1016/j.biomaterials.2003.09.071.
(76) Darling, A. L.; Sun, W. 3D Microtomographic Characterization of Precision Extruded Poly-ϵ-Caprolactone Scaffolds. *J. Biomed. Mater. Res. B Appl. Biomater.* **2004**, *70B* (2), 311–317. https://doi.org/10.1002/jbm.b.30050.
(77) Jenkins, D.; Salhadar, K.; Ashby, G.; Mishra, A.; Cheshire, J.; Beltran, F.; Grunlan, M.; Andrieux, S.; Stubenrauch, C.; Cosgriff-Hernandez, E. PoreScript: Semi-Automated Pore Size Algorithm for Scaffold Characterization. *Bioact. Mater.* **2022**, *13*, 1–8. https://doi.org/10.1016/j.bioactmat.2021.11.006.
(78) Wang, Z.; Wang, Z. Robust Cell Segmentation Based on Gradient Detection, Gabor Filtering and Morphological Erosion. *Biomed. Signal Process. Control* **2021**, *65*, 102390. https://doi.org/10.1016/j.bspc.2020.102390.
(79) João, A.; Gambaruto, A.; Sequeira, A. Anisotropic Gradient-Based Filtering for Object Segmentation in Medical Images. *Comput. Methods Biomech. Biomed. Eng. Imaging Vis.* **2020**, *8* (6), 621–630.
(80) Mangan, A. P.; Whitaker, R. T. Partitioning 3D Surface Meshes Using Watershed Segmentation. *IEEE Trans. Vis. Comput. Graph.* **1999**, *5* (4), 308–321. https://doi.org/10.1109/2945.817348.
(81) Khan, Z. A.; Gostick, J. T. Enhancing Pore Network Extraction Performance via Seed-Based Pore Region Growing Segmentation. *Adv. Water Resour.* **2024**, *183*, 104591. https://doi.org/10.1016/j.advwatres.2023.104591.
(82) Harding, J. L.; Osmond, M. J.; Krebs, M. D. Engineering Osteoinductive Biomaterials by Bioinspired Synthesis of Apatite Coatings on Collagen Hydrogels with Varied Pore

View Article Online
DOI: 10.1039/D5TB00848D

Microarchitectures. *Tissue Eng. Part A* **2017**, *23* (23–24), 1452–1465. https://doi.org/10.1089/ten.tea.2017.0031.

(83) Garczyk, Ż.; Jaegermann, Z.; Duda, P.; Swinarew, A. S.; Stach, S. Ceramic Biomaterial Pores Stereology Analysis by the Use of Microtomography. *Materials* **2021**, *14* (9). https://doi.org/10.3390/ma14092207.

(84) Maleki, B.; Tabandeh, F.; Soheili, Z.-S.; Morshedi, D. Application of Proteinous Nanofibrils to Culture Retinal Pigmented Epithelium Cells: A Versatile Biomaterial. *React. Funct. Polym.* **2017**, *115*, 36–42. https://doi.org/10.1016/j.reactfunctpolym.2017.03.011.

(85) Guével, A.; Rattez, H.; Veveakis, E. Morphometric Description of Strength and Degradation in Porous Media. *Int. J. Solids Struct.* **2022**, *241*, 111454. https://doi.org/10.1016/j.ijsolstr.2022.111454.

(86) Ávila, J.; Pagalo, J.; Espinoza-Andaluz, M. Evaluation of Geometric Tortuosity for 3D Digitally Generated Porous Media Considering the Pore Size Distribution and the A-Star Algorithm. *Sci. Rep.* **2022**, *12* (1), 19463. https://doi.org/10.1038/s41598-022-23643-6.

(87) Paruchuri, A.; Wang, Y.; Gu, X.; Jayaraman, A. Machine Learning for Analyzing Atomic Force Microscopy (AFM) Images Generated from Polymer Blends. *Digit. Discov.* **2024**, *3* (12), 2533–2550. https://doi.org/10.1039/D4DD00215F.

(88) Polez, R. T.; Ajiboye, M. A.; Österberg, M.; Horn, M. M. Chitosan Hydrogels Enriched with Bioactive Phloroglucinol for Controlled Drug Diffusion and Potential Wound Healing. *Int. J. Biol. Macromol.* **2024**, *265*, 130808. https://doi.org/10.1016/j.ijbiomac.2024.130808.

(89) Ibanez, L.; Schroeder, W.; Ng, L.; Cates, J. *The ITK Software Guide*; Kitware Clifton Park, NY, 2005; Vol. 2.

(90) Efraim, Y.; Schoen, B.; Zahran, S.; Davidov, T.; Vasilyev, G.; Baruch, L.; Zussman, E.; Machluf, M. 3D Structure and Processing Methods Direct the Biological Attributes of ECM-Based Cardiac Scaffolds. *Sci. Rep.* **2019**, *9* (1), 5578. https://doi.org/10.1038/s41598-019-41831-9.

(91) Tourlomousis, F.; Boettcher, W.; Ding, H.; Chang, R. C. *Investigation of Cellular Confinement in 3D Microscale Fibrous Substrates: Fabrication and Metrology*; International Manufacturing Science and Engineering Conference; 2017; Vol. Volume 4: Bio and Sustainable Manufacturing. https://doi.org/10.1115/MSEC2017-3020.

(92) Sampson, W. W. *Modelling Stochastic Fibrous Materials with Mathematica®*; Springer Science & Business Media, 2008.

(93) Mndlovu, H.; Kumar, P.; du Toit, L. C.; Choonara, Y. E. A Review of Biomaterial Degradation Assessment Approaches Employed in the Biomedical Field. *Npj Mater. Degrad.* **2024**, *8* (1), 66. https://doi.org/10.1038/s41529-024-00487-1.

(94) Shi, X.; Misch, D.; Vranjes-Wessely, S. A Comprehensive Assessment of Image Processing Variability in Pore Structural Investigations: Conventional Thresholding vs. Machine Learning Approaches. *Gas Sci. Eng.* **2023**, *115*, 205022. https://doi.org/10.1016/j.jgsce.2023.205022.

(95) Capulli, A. K.; Emmert, M. Y.; Pasqualini, F. S.; Kehl, D.; Caliskan, E.; Lind, J. U.; Sheehy, S. P.; Park, S. J.; Ahn, S.; Weber, B.; Goss, J. A.; Hoerstrup, S. P.; Parker, K. K. JetValve: Rapid Manufacturing of Biohybrid Scaffolds for Biomimetic Heart Valve Replacement. *Biomaterials* **2017**, *133*, 229–241. https://doi.org/10.1016/j.biomaterials.2017.04.033.

(96) Podichetty, J. T.; Madihally, S. V. Modeling of Porous Scaffold Deformation Induced by Medium Perfusion. *J. Biomed. Mater. Res. B Appl. Biomater.* **2014**, *102* (4), 737–748. https://doi.org/10.1002/jbm.b.33054.

(97) Takahashi, A.; Kita, R.; Shinozaki, T.; Kubota, K.; Kaibara, M. Real Space Observation of Three-Dimensional Network Structure of Hydrated Fibrin Gel. *Colloid Polym. Sci.* **2003**, *281* (9), 832–838. https://doi.org/10.1007/s00396-002-0839-0.
(98) Nyberg, E.; O'Sullivan, A.; Grayson, W. scafSLICR: A MATLAB-Based Slicing Algorithm to Enable 3D-Printing of Tissue Engineering Scaffolds with Heterogeneous Porous Microarchitecture. *PLOS ONE* **2019**, *14* (11), 1–17. https://doi.org/10.1371/journal.pone.0225007.
(99) Fantini, M.; Curto, M. Interactive Design and Manufacturing of a Voronoi-Based Biomimetic Bone Scaffold for Morphological Characterization. *Int. J. Interact. Des. Manuf. IJIDeM* **2018**, *12* (2), 585–596. https://doi.org/10.1007/s12008-017-0416-x.
(100) Jiao, Y.; Torquato, S. Quantitative Characterization of the Microstructure and Transport Properties of Biopolymer Networks. *Phys. Biol.* **2012**, *9* (3), 036009. https://doi.org/10.1088/1478-3975/9/3/036009.
(101) Naing, M. W.; Chua, C. K.; Leong, K. F.; Wang, Y. Fabrication of Customised Scaffolds Using Computer-aided Design and Rapid Prototyping Techniques. *Rapid Prototyp. J.* **2005**, *11* (4), 249–259.
(102) Münster, S.; Fabry, B. A Simplified Implementation of the Bubble Analysis of Biopolymer Network Pores. *Biophys. J.* **2013**, *104* (12), 2774–2775. https://doi.org/10.1016/j.bpj.2013.05.016.
(103) Molteni, M.; Magatti, D.; Cardinali, B.; Rocco, M.; Ferri, F. Response to "A Simplified Implementation of the Bubble Analysis of Biopolymer Networks Pores." *Biophys. J.* **2013**, *104* (12), 2776–2777. https://doi.org/10.1016/j.bpj.2013.05.015.
(104) Grabska-Zielińska, S.; Sionkowska, A.; Reczyńska, K.; Pamuła, E. Physico-Chemical Characterization and Biological Tests of Collagen/Silk Fibroin/Chitosan Scaffolds Cross-Linked by Dialdehyde Starch. *Polymers* **2020**, *12* (2). https://doi.org/10.3390/polym12020372.
(105) Agarwal, G.; Agrawal, A. K.; Fatima, A.; Srivastava, A. X-Ray Tomography Analysis Reveals the Influence of Graphene on Porous Morphology of Collagen Cryogels. *Micron* **2021**, *150*, 103127. https://doi.org/10.1016/j.micron.2021.103127.
(106) Arbez, B.; Kün-Darbois, J.-D.; Convert, T.; Guillaume, B.; Mercier, P.; Hubert, L.; Chappard, D. Biomaterial Granules Used for Filling Bone Defects Constitute 3D Scaffolds: Porosity, Microarchitecture and Molecular Composition Analyzed by microCT and Raman Microspectroscopy. *J. Biomed. Mater. Res. B Appl. Biomater.* **2019**, *107* (2), 415–423. https://doi.org/10.1002/jbm.b.34133.
(107) Wei, H.-J.; Liang, H.-C.; Lee, M.-H.; Huang, Y.-C.; Chang, Y.; Sung, H.-W. Construction of Varying Porous Structures in Acellular Bovine Pericardia as a Tissue-Engineering Extracellular Matrix. *Biomaterials* **2005**, *26* (14), 1905–1913. https://doi.org/10.1016/j.biomaterials.2004.06.014.
(108) Zang, C.; Che, M.; Xian, H.; Xiao, X.; Li, T.; Chen, Y.; Liu, Y.; Cong, R. 3D-Printed Silicate Porous Bioceramics Promoted the Polarization of M2-Macrophages That Enhanced the Angiogenesis in Bone Regeneration. *J. Biomed. Mater. Res. B Appl. Biomater.* **2024**, *112* (9), e35469. https://doi.org/10.1002/jbm.b.35469.
(109) Guo, Y.; Chen, Z.; Wen, J.; Jia, M.; Shao, Z.; Zhao, X. A Simple Semi-Quantitative Approach Studying the in Vivo Degradation of Regenerated Silk Fibroin Scaffolds with Different Pore Sizes. *Mater. Sci. Eng. C* **2017**, *79*, 161–167. https://doi.org/10.1016/j.msec.2017.05.008.
(110) Liu, E.; Treiser, M. D.; Johnson, P. A.; Patel, P.; Rege, A.; Kohn, J.; Moghe, P. V. Quantitative Biorelevant Profiling of Material Microstructure within 3D Porous Scaffolds via Multiphoton Fluorescence Microscopy. *J. Biomed. Mater. Res. B Appl. Biomater.* **2007**, *82B* (2), 284–297. https://doi.org/10.1002/jbm.b.30732.

(111) Lindström, S. B.; Vader, D. A.; Kulachenko, A.; Weitz, D. A. Biopolymer Network Geometries: Characterization, Regeneration, and Elastic Properties. *Phys Rev E* **2010**, *82* (5), 051905. https://doi.org/10.1103/PhysRevE.82.051905.

(112) Haeri, M.; Haeri, M. ImageJ Plugin for Analysis of Porous Scaffolds Used in Tissue Engineering. *J. Open Res. Softw.* **2015**. https://doi.org/10.5334/jors.bn.

View Article Online
DOI: 10.1039/D5TB00848D

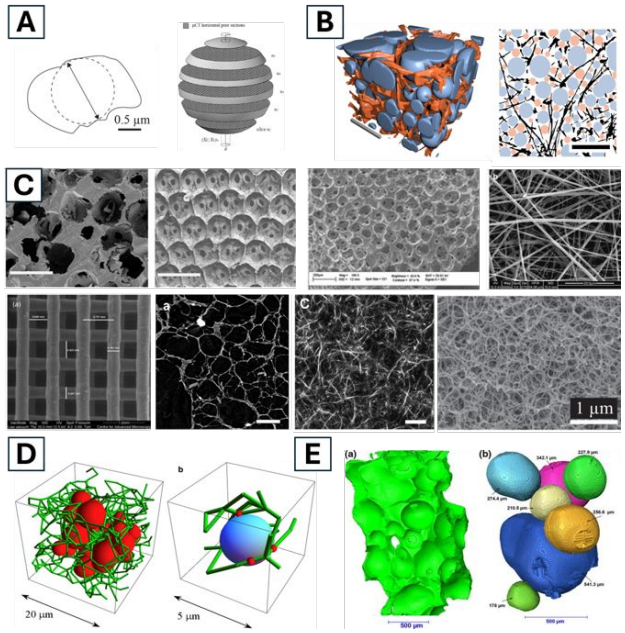

Figure 1: 2D and 3D pore architectures in biomaterials.
All images have been reproduced with permission.
A: Left: How a pore is defined in a 2D image[2]. Right: Graphical representation of pore size calculation and slices used in a 3D reconstruction[45].
B: Left: 3D visualisation of pores detected as spherical bubbles: Orange depicts segmented collagen fibers and blue represents pores. Right: 2D visualisation (circles) of detected 3D bubbles in the left image, in an exemplary 2D image slice. Black depicts segmented collagen fibers, blue represents determined pores of a single analysis process, orange represents detected pores of a second residual analysis[16].
C: Top left corner and centre: Scanning electron microscopy (SEM) images of salt leached and gas foamed scaffolds[3]. Top right centre: Scanning electron micrograph of the microfluidic foaming poly(vinyl alcohol) (PVA) scaffold[45]. Top right corner: FESEM images of electrospun poly(l-lactic acid)-co-poly(ε-caprolactone)-Gelatin (PLACL/Gel) nanofibers[37]. Bottom left corner: SEM micrographs of a PCL scaffolds produced by bioextrusion[15]. Bottom left centre: Micro-CT 2D section of a collagen-based composite scaffold[46]. Bottom right centre: Confocal fluorescence microscopy image of a collagen network[47]. Bottom right corner: SEM image of an agarose hydrogel[2].
D: 3D bubble method applied to an in silico fibrin gel. Left: Red spheres represent the largest 3D bubbles that can be optimally fit in the pore zones of the gel and produce their maximum filling. Right: Zoom of a single sphere touching four different fibers[17].
E: Left: Synchroton micro-CT image of a bioactive glass scaffold. Right: Pores within the scaffold identified by image analysis algorithms[48].

View Article Online
DOI: 10.1039/D5TB00848D

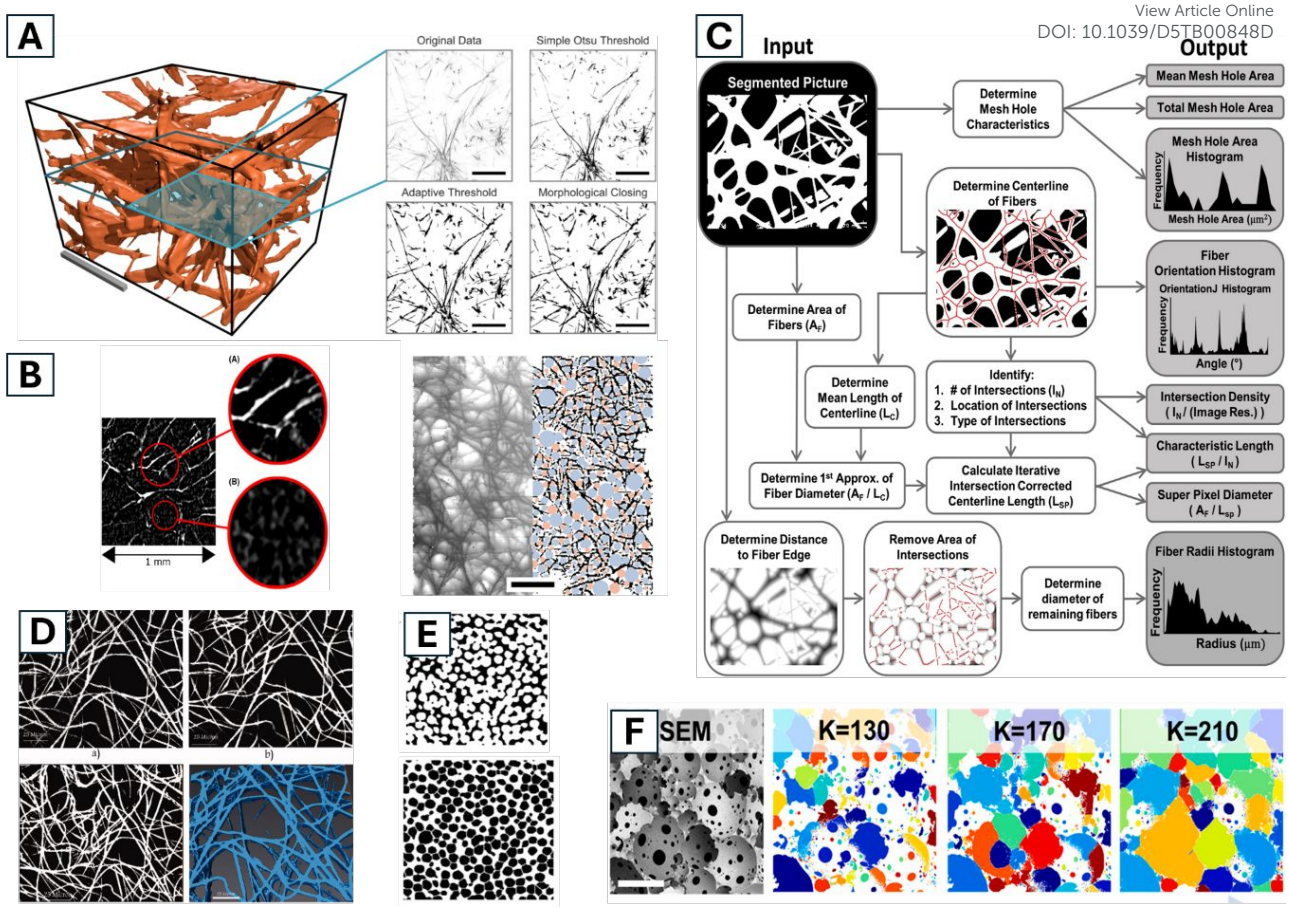

Figure 2: Examples of segmentation methods.
All images have been reproduced with permission.
A: 3D collagen network binarisation method. Left: Representative image cube of a 5(6)-Carboxytetramethylrhodamine N-succinimidylester (TAMRA)-labelled collagen scaffold. Right: A representative 2D slice of original image data, Otsu's thresholding, adaptive local thresholding of a denoised and the final segmentation result[16].
B: An unthresholded, undespeckled section of a micro-CT image of a collagen scaffold, demonstrating the noise which can be present in this type of data. Top right: Shows collagen in white, with the noise manually removed. Black represents void. Bottom right: shows the isolated noise, seen as light grey specks[57].
C: Overview of how the DiameterJ algorithm analyses fiber diameter and other scaffold properties[56].
D: Top left: CLSM images of nanomicrofiber scaffolds. Top right: filtered with median 3D. Bottom left: binarised. Bottom right: 3D reconstructed with Avizo Fire software[43].
E: Top: Binarised image of a PVA scaffold. Bottom: Separation of pores using the watershed algorithm[45].
F: Effect of pixel intensity threshold, K, on pore identification and resulting effect on pore size of scaffolds[3].

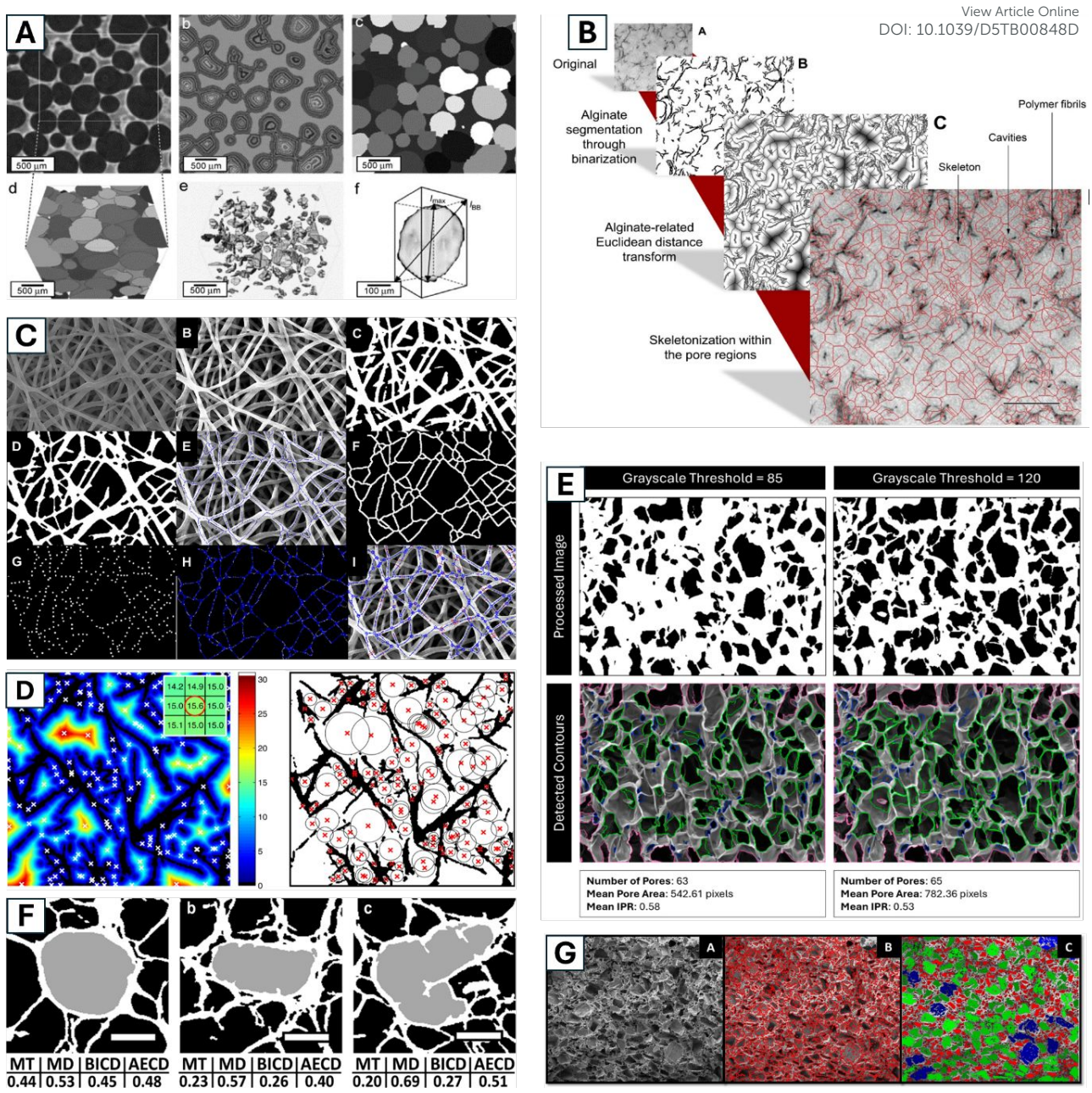

Figure 3: Examples of automated pore size determination methods.
All images have been reproduced with permission.
A: Quantification of 3D pore networks of sol–gel derived bioactive glass foams from micro-CT data: (a) 2D slice of raw data, (b) 2D slice showing application of the dilation algorithm, (c) 2D representation of pores derived from the watershed algorithm, (d) 3D image of identified pores, (e) 3D image of the interconnects obtained from the top down algorithm, and (f) demonstration of the bounding box method of measuring the interconnect length[19].
B: Illustration of pore size determination of alginate hydrogel microcapsules using TEM images. Image A depicts a hydrogel as it is typically observed using transmission electron microscopy. Image B shows the results of the image segmentation after binarisation. Image C shows the result of a Euclidean distance transformation. Image D gives an overlay of the pore region image skeleton (red lines) with the original image. Image skeletons are one-pixel wide

View Article Online
DOI: 10.1039/D5TB00848D

center axes. They are defined via the set of inner pore pixels. The set is defined via local distance maxima with respect to alginate segments[38].

C: Fiber network diameter determination of scaffolds (opposite of pore size determination, using similar algorithms). Top left: starting SEM image. Top centre: image histogram equalsation followed by 3 by 3 median filtering. Top right: local thresholding through Otsu method. Middle left: thinning, smoothing and removal of isolated pixel areas through a cascade of different morphological operators. Middle center: skeletonization. Middle right – Bottom left: binary filters for Delaunay network refinement. Bottom center: modified Delaunay network associated to the real fiber network. Bottom right: final network and fiber diameters detected[25].

D: Simplified bubble analysis of the pore space of a random biopolymer network in two steps. Left: first, the Euclidean distance map (EDM) of the fluid space of the network structure is computed (shades of gray (colours online) indicate the distance of each fluid pixel to the nearest fiber pixel). (Black) Fibers. Second, the local maxima of the EDM (white crosses) determine the centres of all 2D bubbles. To avoid bubbles of similar size in close proximity, the EDM was smoothed with a 5 × 5 Gaussian kernel with a sigma of one before the local maxima were determined. (Inset) A local maximum of the EDM (red circle) is a pixel whose eight neighbours all have smaller values. Right: Resulting 2D bubbles (black circles) fit into the pore zones of the fiber structure (black). (Red crosses) Bubble centers[102].

E: Comparison of detected pores with cutoff values of 85 vs. 120 in Chitosan-gelatin cryogels using PoreVision software. Red outlines are pores outside the analysis boundary, blue outlines are pores removed for being too small (most likely dust, cracks, or folds), and green outlines are identified pores[20].

F: Illustration of varying results provided by micro-CT 2D pore size analysis of collagen-based scaffolds. Pores (in gray) of 3 differing shapes (left, centre, right) were evaluated by means of 4 micro-CT 2D parameters (MT—mean thickness, MD—major diameter, BICD—biggest inner circle diameter, AECD—area-equivalent circle diameter) and their values are presented in panels below the images (in mm). The results tend to differ with increasing shape irregularity[46].

G: Colour map and pixel intensity based measurement of macro pore size distribution in a polymeric scaffold[21].

Automated Analysis of Pore Structures in Biomaterials - Data Availability Statement

View Article Online
DOI: 10.1039/D5TB00848D

Nicola Rossberg[1], Simon Corrie[2], Lisbeth Grøndahl[3] and Imanda Jayawardena[4]*

1. Taighde Éireann - Research Ireland Center for Research Training in Artificial Intelligence, School of Computer Science & Information Technology, University College Cork, Co. Cork T12 K8AF, Ireland.
2. Chemical and Biological Engineering Department, ARC Centre of Excellence in Carbon Science and Innovation, Monash University, Clayton, VIC 3800, Australia.
3. School of Chemistry and Molecular Biosciences, University of Queensland, Brisbane, QLD 4072, Australia.
4. Tyndall National Institute, Lee Maltings Complex, Dyke Parade, Cork, Co. Cork T12R5CP, Ireland.

No primary research results, software or code have been included and no new data were generated or analysed as part of this perspective.